William V. Mars,[1,3] Govind Paudel,[2] Jesse D. Suter,[1] and Christopher G. Robertson[1]

Incremental, Critical Plane Analysis of Standing Wave Development, Self-Heating, and Fatigue during Regulatory High-Speed Tire Testing Protocols

REFERENCE: Mars, W. V., Paudel, G., Suter, J. D., and Robertson, C. G., **"Incremental, Critical Plane Analysis of Standing Wave Development, Self-Heating, and Fatigue during Regulatory High-Speed Tire Testing Protocols,"** *Tire Science and Technology,* TSTCA, Vol. 49, No. 3, July–September 2021, pp. 172–205.

ABSTRACT: Tire speed ratings derive from regulatory testing in which tire structural integrity is validated over a series of steps with successively increasing speed. For the FMVSS 139 high-speed standard, there are four half-hour duration speed steps at 80, 140, 150, and 160 kph. Speed ratings from Q through Y may be attained through the UN ECE R30 regulation high-speed testing. For either protocol, a tire must demonstrate the ability to operate without crack development at high speed for a specified period. After the test, "there shall be no evidence of tread, sidewall, ply, cord, inner liner, belt or bead separation, chunking, broken cords, cracking, or open splices." A workflow for simulating regulatory high-speed durability performance has been developed based upon (1) recent improvements to the Abaqus steady-state transport formulation that now permit converged solutions to be obtained at high speed (including after the development of standing waves in the tire) and (2) Endurica DT self-heating and incremental fatigue simulations that account for thermal effects and for damage accumulation occurring due to a schedule of load cases. The self-heating calculation features the Kraus model and accurately captures viscoelastic loss modulus dependence on strain amplitude and temperature. For each step of the high-speed procedure, steady-state structural and thermal solutions are first computed. The deformation history in the presence of standing waves is shown to require rainflow counting due to the occurrence of multiple load cycles per tire revolution. Crack growth is finally integrated for each potential critical plane through each step of the test until failure is indicated. Standing waves at high speed induce significant self-heating and damage, rapidly limiting high-speed performance. The temperature dependence of self-heating and strength properties also plays a major role in limiting high-speed durability. The simulations were executed on both a flat surface and on the regulation specified 1.7 m diameter road wheel. As expected, durability testing on the road wheel is more severe, and the beneficial effect of a nylon overwrap is predicted.

KEY WORDS: durability, high speed, fracture mechanics, FMVSS 139, UN ECE R30

Introduction

Durability standards in the tire industry often specify a multistep testing format in which the subject tire is operated over a prescheduled series of

[1] Endurica LLC, 1219 West Main Cross, Suite 201, Findlay, Ohio 45840, USA. Email: wvmars@endurica.com

[2] Dassault Systemes, 6105 Parkland Boulevard, Mayfield Heights, Ohio 44124, USA

[3] Corresponding author

TABLE 1 — *Multistep durability testing protocol combining the FMVSS 139 high-speed requirement and the UN ECE R30 speed rating test.*

Step, rating	Load (% TRA)	Speed (kph)	Initial inflation (kPa)	Step duration (min)
1 FMVSS 139	85	80	220	120
2 FMVSS 139	85	140	220	30
3 FMVSS 139	85	150	220	30
4 FMVSS 139	85	160	220	30
5 EC 30, Q	100	160	220	10
6 EC 30, R	100	170	220	10
7 EC 30, S	100	180	220	10
8 EC 30, T	100	190	220	10
9 EC 30, U	100	200	220	10
10 EC 30, H	100	210	220	10
11 EC 30, V	100	240	220	10
12 EC 30, W	85	270	220	10
13 EC 30, Y	85	300	220	10

increasingly severe conditions. In order to legally qualify as a "safe" tire, the standards [*1*,*2*] specify that there "shall be no visual evidence of tread, sidewall, ply, cord, inner liner, or bead separation, chunking, broken cords, cracking, or open splices." For example, the high-speed tests specified in the FMVSS 139 regulation and in the UN ECE R30 regulation both involve multiple steps of increasing tire speed. The three-step durability test with increasing load, specified in FMVSS 119, is another example. For tires that pass these minimum requirements with no obvious damage, it is also possible for tire makers to augment the regulation testing schedules with additional steps at over-load and/or over-speed conditions. Probing the ultimate limits of the tire's capacity gives engineers evidence to support development program imperatives to maintain or enhance durability performance.

In contrast, tire durability simulations have traditionally been abbreviated to a single operating condition [*3*–*11*]. This simplification reduces analysis complexity and cost while still providing a form of relative guidance, but it gets in the way of matching up simulation results with regulatory test results. The aim of this work is to establish and demonstrate durability simulation procedures that address the multistep features of the regulatory testing protocols and provide insights into the effects of the progression of damage during the test.

The procedures are specified in Table 1. This protocol combines the FMVSS 139 high-speed requirement [*1*] and the UN ECE R30 speed rating test [*2*]. The subject tire has size P195/85R17 with a Tire & Rim Association (T&RA) 100% load of 8380 N under 220 kPa of controlled inflation pressure. The tire was modeled at steady-state rolling on both a 1.7 m road wheel and on a flat road surface.

The analysis begins by obtaining finite element solutions for the steady-state rolling tire at each step of Table 1. For each step, both a structural and a thermal solution were computed. Because of high speeds, it was necessary for the structural solution to capture standing waves [*12–16*]. The steady-state solutions were obtained using Abaqus 2019, which features enhanced convergence for rolling structures at high speed. The dissipation field used in computing the thermal solution was generated in Endurica CL using the Kraus model of loss modulus dependence on strain amplitude, with account taken of the temperature dependence of viscoelastic dissipation. Finally, the damage occurring during each test step was accrued using the Endurica DT incremental fatigue solver. The dependence of the crack growth rate law on temperature was considered using the table-lookup functionality provided by Endurica DT.

Steady-State Rolling Structural Analysis

Stress–Strain Behavior

The neo-Hookean stress–strain law was used for the sake of simplicity in specifying material behavior and in light of the fact that operating strains in the tire are generally modest. The neo-Hookean strain energy potential W is defined in terms of the material parameters C_{10}, and D_1 and the principal stretches λ_1, λ_2, and λ_3,

$$W_{\text{neo}} = C_{10}(\lambda_1^2 + \lambda_2^2 + \lambda_3^2 - 3) + \frac{1}{D_1}(J^{\text{el}} - 1)^2 \tag{1}$$

J^{el} is the elastic volume ratio.

The material parameter C_{10} is listed in the Table 2, while the parameter D_1 is chosen such that Poisson's ratio is 0.495.

The belts and the plies were represented via the Marlow [*17*] stress–strain law, which enabled a tabular specification of the nonlinear elastic stress–strain curve. A linear elastic model was used to represent the bead wire.

Model Details

A P195/75R17 grooved symmetric tire is used to carry out all the simulations. A cross-sectional view with the finite element mesh, overall dimensions, and a detail construction of the tire is shown in Figs. 1 and 2.

The axisymmetric finite element model uses all rubber compounds described in Table 2 as solid elements including the bead wire. The plies, the belts, and the overwrap are modeled as surface elements, which are then embedded into the solid elements.

In order to simplify the model, a rigid body constraint is applied to represent the tire rim. The highlighted nodes of the tire carcass in Fig. 3 are used to form a rigid body constraint with the rim axle located at the center of the axis of revolution.

TABLE 2 — *Material properties of structural analysis.*

No.	Name	Material	C_{10} (Mpa)	D_1 (Mpa)	E (Mpa)	EPI	Angle (°)	Density (g/cm^3)
1	Inner liner	Rubber	0.64	0.0158	—	—	—	1.1
2	Abrasion	Rubber	1.71	0.0059	—	—	—	1.1
3	Bead	Steel	—	—	135 000	—	—	7.5
4	Apex	Rubber	3.63	0.0028	—	—	—	1.1
5	Shoulder	Rubber	1.79	0.0056	—	—	—	1.1
6	Body ply	Nylon	—	—	4600[a]	14	0	1.3
7	Ply gum	Rubber	1.79	0.0056	—	—	—	1.1
8	Edge cover	Rubber	4.06	0.0025	—	—	—	1.1
9	Tread	Rubber	1.04	0.0096	—	—	—	1.1
10	Inner belt	Steel	—	—	76 000[a]	17	25	7.5
11	Outer belt	Steel	—	—	76 000[a]	17	−25	7.5
12	Belt gum	Rubber	4.06	0.0025	—	—	—	1.1
13	Overwrap	Nylon			4600[a]	17	90	1.3
14	Tread base	Rubber	4.06	0.0025	—	—	—	1.1

[a]Body ply, belts, and overwrap use surrogate test data and Marlow strain energy potential.

A simulation was set up to inflate the tire to 220 kPa pressure in the axisymmetric model. The simulation results from the inflation analysis were transferred to the three-dimensional (3D) tire model using the symmetric model generation and the symmetric results transfer technique available in Abaqus. This technique generates a 3D tire mesh from the axisymmetric model with user defined discretization along the circumference of the tire. A uniform angle of 3° sectors was created around the circumference of the tire as shown in Fig. 4. Although it is common to focus circumferential refinement in the tire footprint for steady-state analyses, in the present work the uniform mesh was specified in order to properly resolve standing waves.

The 3D tire model was set up to simulate the footprint analysis with two different load cases: 8380 N (1884 lbf) and 7123 N (1601 lbf). These loads were taken from the T&RA handbook representing 100% and 85 % of rated

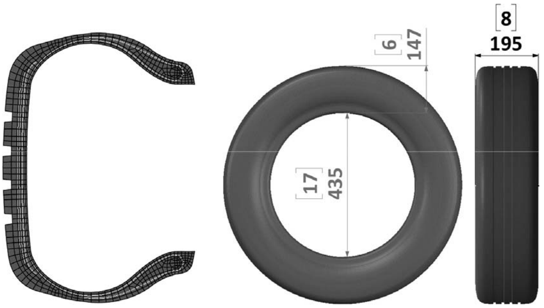

FIG. 1 — *Cross-sectional view and overall dimensions in mm [inches].*

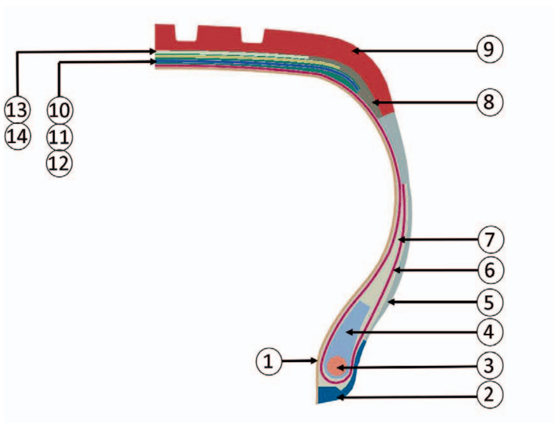

No	Name
1	Inner liner
2	Abrasion
3	Bead
4	Apex
5	Shoulder
6	Body ply
7	Ply gum
8	Edge cover
9	Tread
10	Inner belt
11	Outer belt
12	Belt gum
13	Overwrap
14	Tread base

FIG. 2 — *Construction details of subject tire.*

load, respectively. The footprint analysis was conducted initially on a 1.7 m diameter drum as shown in Fig. 4. The drum is modeled as a rigid surface, and the contact between the tire and the drum was modeled with a coulomb friction coefficient of 0.8.

Additional simulations were also performed by replacing the drum with a flat surface to quantify the impact of roadwheel curvature on tire damage.

The 3D loaded tire was used to perform the steady-state rolling analysis under the speeds listed in Table 1.

Steady-State Rolling Theory

Simulation of dynamics of a tire using the steady-state rolling theory is frequently carried out using Abaqus: A Dassault Systemes Simulia brand finite element code [*18–22*]. A general purpose, steady-state transport theorem implemented in Abaqus makes it possible to simulate most of the tire rolling phenomena that exhibit steady-state behavior such as rolling on a drum or on a

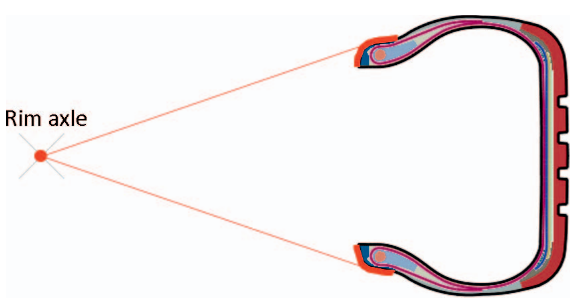

FIG. 3 — *Tire rim representation with a rigid body constraint.*

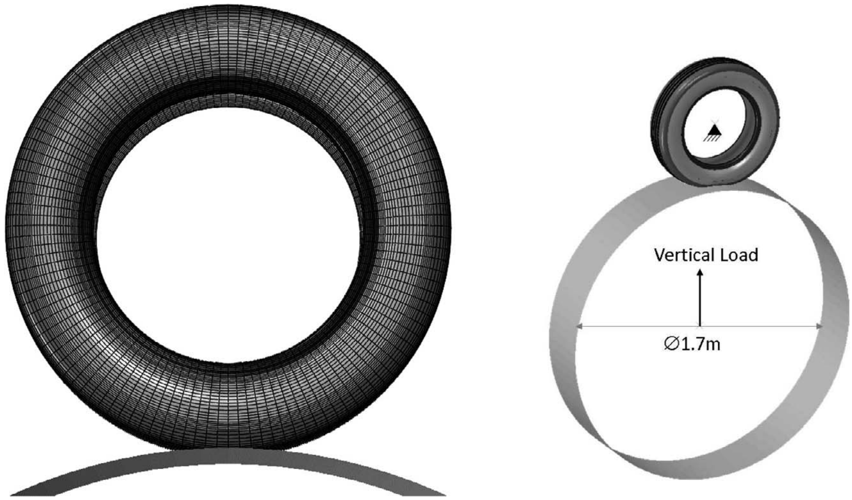

FIG. 4 — *3D finite element mesh and footprint setup.*

flat surface. The alternative to the steady-state rolling is to use either a transient implicit or an explicit rolling simulation. However, the cost of the implicit and the explicit rolling, in both the fidelity of the finite element model and the simulation runtime, makes these approaches impractical.

Steady-state transport analysis takes advantage of the fact that a steady-state solution is possible for a tire that is traveling at a constant ground velocity and a constant angular rolling velocity. The steady-state transport analysis uses a reference frame attached to the axle of the tire. This special reference frame removes explicit time dependence from the problem, so that a purely spatially dependent analysis can be performed. The finite element mesh describing the tire in this frame of reference remains stationary. This kinematic description can be viewed as a mixed Eulerian/Lagrangian formulation, where the rigid body rotation is described in an Eulerian manner and the deformation is measured in a Lagrangian manner.

Consider the case shown in Fig. 5(a), where a cylindrical body is rotating with a constant angular rolling velocity $\boldsymbol{\omega}$ around a rigid axle $\boldsymbol{T}$ at $\boldsymbol{X_0}$, which in turn rotates with constant angular velocity $\boldsymbol{\Omega}$ around the fixed cornering axis $\boldsymbol{n}$ through point $\boldsymbol{X_c}$ [*22*].

The velocity $\boldsymbol{v_r}$ and the acceleration $\boldsymbol{a_r}$ in the reference frame for the steady-state conditions can be expressed as:

$$v_r = \Omega \boldsymbol{n} \times (x - X_c) + \omega R \frac{\partial X}{\partial S} \tag{2}$$

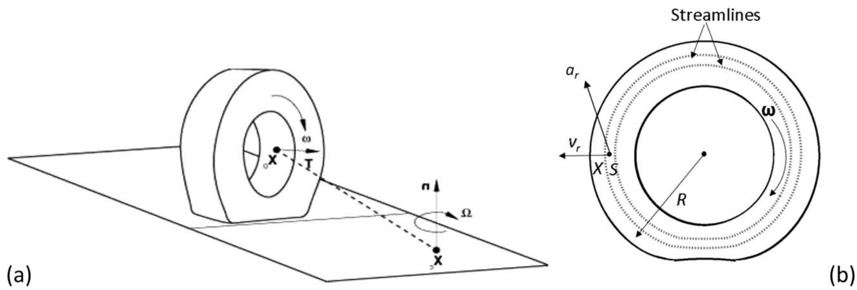

FIG. 5 — *Steady-state rolling (a) cornering and (b) straight-line rolling.*

$$a_r = \Omega^2(\boldsymbol{nn} - \boldsymbol{I}) \cdot (x - X_c) + 2\omega\ \Omega\ R\boldsymbol{n} \times \frac{\partial X}{\partial S} + \omega^2 R^2 \frac{\partial^2 X}{\partial S^2} \tag{3}$$

where S is the coordinate of point X along the streamline, and R is the radius of the point on the reference body from the axle of the tire. For a straight-line rolling as shown in Fig. 5b, the above expression is reduced to

$$v = \omega R \frac{\partial X}{\partial S} \tag{4}$$

$$a = \omega^2 R^2 \frac{\partial^2 X}{\partial S^2} \tag{5}$$

The acceleration expression in Eq. (5) includes the inertial effect coming from both the Coriolis and the centrifugal forces. The inertial effect is calculated from the external virtual work δW^{ext}, which is derived from the d'Alembert forces,

$$\partial W^{\text{ext}} = -\int_{V_0} \rho_0 a \cdot \partial v dV_0 \tag{6}$$

where ρ_0 is the mass density of the material and V is the volume of the reference body.

The inertial forces are evaluated along the streamlines of the rolling tire by using standard Galerkin methods. However, when the inertial forces become significant, at higher rolling speeds, the solution starts to diverge as the tire becomes unstable at the onset of the standing waves. A recent development in Abaqus steady-state transport analysis addresses this divergence problem by introducing a weighted shape function in the Galerkin methods. This improved shape function allows a nonuniform convection of the inertial forces along the circumference: from the leading edge to the trailing edge of the tire. As a result,

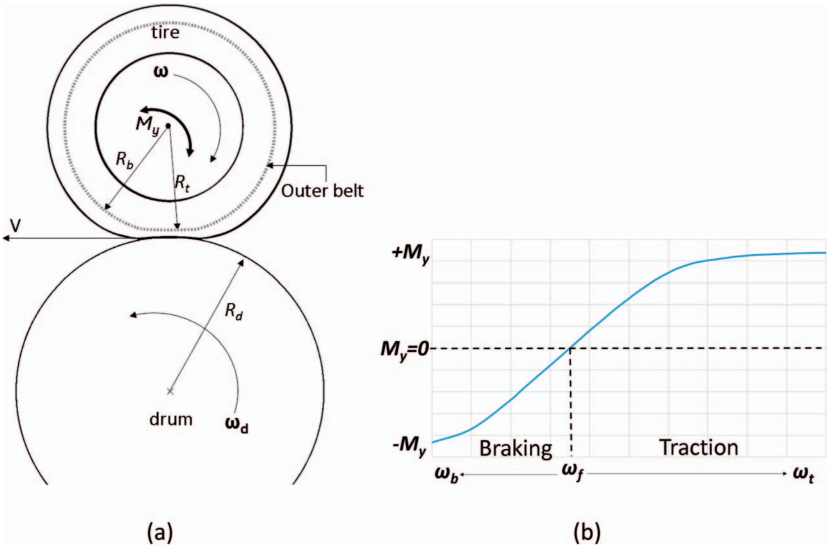

FIG. 6 — *Free rolling condition (a) model setup and (b) braking and traction state.*

convergence during high-speed rolling can be achieved at and beyond the point where standing waves occur in the tire.

Since the tire is not explicitly rotating in the steady-state transport analysis, both the ground velocity V and the rolling angular speed ω must be prescribed as shown in Fig. 6a. A free rolling solution is obtained at the angular speed, ω_f, where the torque about the axle of the tire M_y is zero.

$$\omega_f = \frac{V}{R_f} \tag{7}$$

where R_f is the free rolling radius of the tire and it is not known in advance. The radius of the outermost belt is used to calculate the free rolling radius such that $\boldsymbol{R_b > R_f > R_t}$, where R_b is the inflated but unloaded belt radius and R_t is the loaded belt radius. Therefore for a given ground speed V, the angular speed ω is ramped from $\omega_b(V/R_b)$ to $\omega_t(V/R_t)$ so that the tire transitions from the full braking state to the full traction state. As a result, the free rolling speed ω_f is determined where $M_y = 0$ as shown in Fig. 6b.

Structural Analysis Workflow

The overall workflow for the structural analyses is shown in Fig. 7. This procedure was executed for each step of the testing protocol. All analyses originated from the same inflation job. Two static footprint jobs were then made, one at 85% load and the other at 100% load. The steady-state rolling procedure for each speed was then started from the static footprint job and

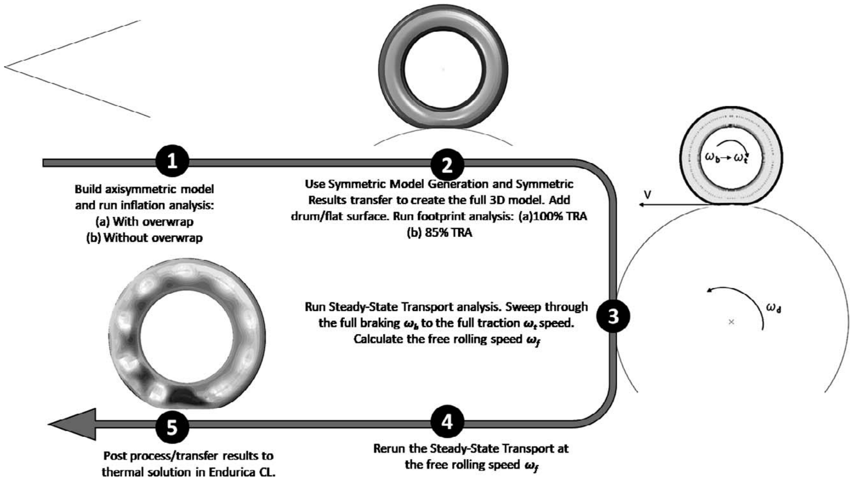

FIG. 7 — *Steady-state rolling modeling workflow.*

equilibrated at the free rolling condition, resulting ultimately in a separate converged solution for each step of the protocol.

Structural Results

A first manifestation of the inertial effects of steady-state rolling is growth of the free rolling radius of the tire. The free rolling radius R_f is computed from Eq. (7), V is specified, ω_f is determined by the finite element solution as the angular speed that results in zero driving or braking torque. The free rolling radius is plotted on a per step basis in Fig. 8, and as a function of speed in Fig. 9. The free rolling radius on the 1.7 m road wheel is smaller than on a flat surface at constant load, reflecting lower stiffness and larger deflection. The drum and flat results were computed with the nylon overwrap layer specified in Table 2. The no overwrap case was computed for a flat surface by removing the overwrap rebar layer from the model.

A second manifestation of inertial effects is the development of standing waves in the solution at higher speeds. Figure 10 visualizes standing wave development by plotting the out-of-plane displacement U2 at each step of the test. Only the drum case is shown, since the other cases were quite similar. The standing wave first becomes obvious in step 10 at 210 kph. The occurrence of a standing wave multiplies the number of cycles occurring per tire revolution. Where below the standing wave speed there is a single load cycle per revolution associated with material passage through the footprint, once the standing wave develops, the number of sidewall/tread flex cycles per revolution is multiplied, resulting in much greater self-heating and damage to tire materials.

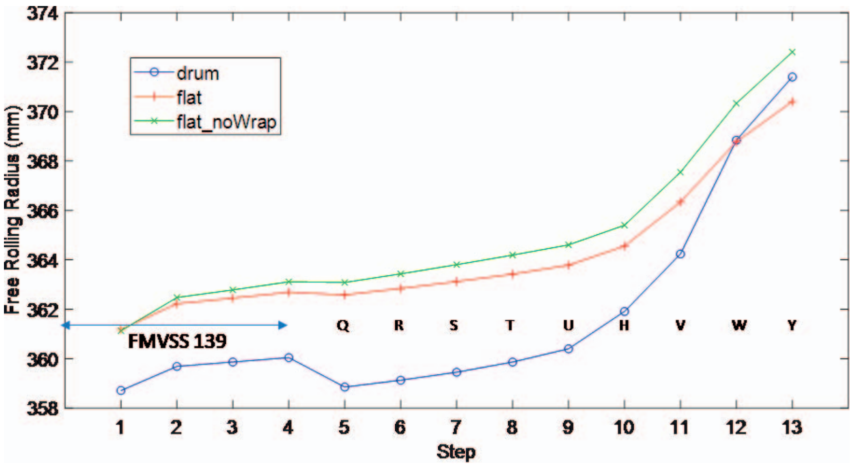

FIG. 8 — *Free rolling radius vs step number. Speed rating symbols are shown corresponding to the respective testing steps.*

Thermal Analysis

In order to assess damage occurring during the testing protocol, the temperature field must be computed. Although a fully transient thermal workflow is possible, for the present study, a steady-state workflow was applied for simplicity. In this workflow, the steady-state thermal solution was obtained for each test step using the already obtained corresponding steady-state structural rolling solution. The rolling resistance of the tire was also computed by integrating the dissipation field over the volume of the tire.

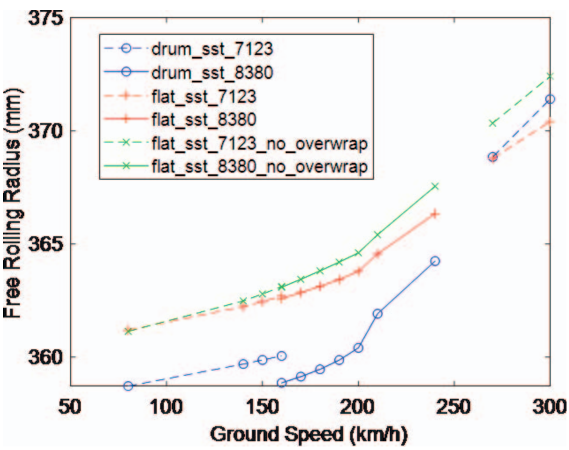

FIG. 9 — *Free rolling radius vs tire speed. Dashed lines represent 85% T&RA load, solid lines represent 100% T&RA load.*

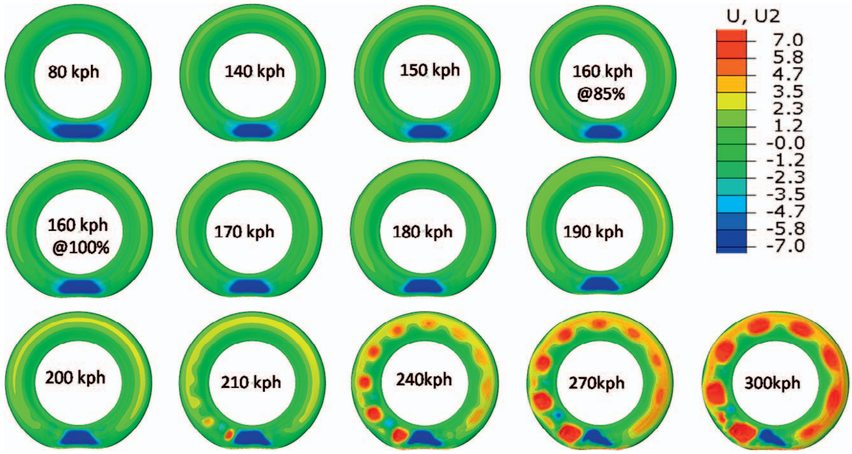

FIG. 10 — *Out-of-plane displacement for tire operating at steady state on 1.7 m road wheel for each speed step.*

Model Details

Temperature was computed on the same two-dimensional (2D) axisymmetric tire cross-section model that was used for mounting and inflation and relying on the usual assumptions [*5*,*8*,*23–27*] that any thermal gradients in the circumferential direction were zero. The 2D model has 1026 elements and 1146 nodes.

The thermal conductivity of all rubber compounds was taken as 0.25 W/(m K) [*28*]. The thermal conductivity of steel was taken as 50 W/(m K).

Two thermal boundary conditions were defined, one for the model exterior free surface (tread and sidewall) and another for the interior surface (inner liner). The exterior surface film coefficient was computed as a function of speed from the relationship for turbulent flow [*24*].

$$h = h_0(R\omega_f/v_0)^{4/5} \tag{8}$$

The value $R = 302$ mm was used as the characteristic radius. The reference speed v_0 was taken as 20 m/s. The reference film coefficient was taken as 83 W/(m^2 K). The sink temperature for external flow was taken as 23 °C.

The interior film coefficient was taken to be constant at a value of 10 W/(m^2 K) with a sink temperature of 40 °C. The assumption of constant film coefficient is founded in the thought that air at steady state in the internal cavity is entrained with the tire and therefore has a small relative velocity.

Dissipation rates for each finite element were computed using the Kraus model in the Endurica CL code's microkinematic hysteresis framework. The

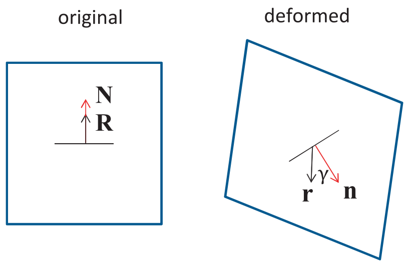

FIG. 11 — *Original and deformed configurations of line and plane elements tracked in a microkinematic analysis. $\vec{R}$ marks the material line segment. $\vec{N}$ marks the material plane. Note that in the undeformed configuration $\vec{N}$ and $\vec{R}$ are coincident unit vectors, but in the deformed configuration their images make an angle according to the amount of shearing γ occurring for the plane specified by $\vec{N}$.*

duration of each tire revolution was specified in the Endurica calculation through the HISTPERIOD parameter, as $P = 2\pi/\omega_f$, where ω_f has units of radians per second.

Microkinematic Dissipation Framework

The Endurica CL microkinematic framework enables the kinematic analysis of material line segments and material planes embedded in a finitely deforming material. Line segments and material planes often hold special physical significance. For example, under affine deformations like that shown in Fig. 11, we may associate a material line segment with the end-to-end distance of a polymer chain. Or we may associate a material plane with a particular microcrack or a specific interface in multiphase material. At a given point of interest in a structure, the microkinetmatic analysis is iterated across all possible orientations of a line segment or material plane for the purpose of accumulating a total material response across all orientations. In the present case, the material response of interest is the total heat energy generated per unit volume due to an applied deformation history.

The length history $|\vec{r}(t)|$ of a unit material line segment $\vec{R}$ specified in the undeformed configuration can be computed from

$$\vec{r} = \overline{\overline{F}}\vec{R} \tag{9}$$

where $\overline{\overline{F}}$ is the deformation gradient.

Likewise, the shearing of a particular material plane, specified in the undeformed configuration by its unit normal $\vec{N}$, can be computed by considering the shear angle history $\gamma(t)$ between the normal of the deformed material plane $\vec{n}$ and the deformed material line $\vec{r}$ that was—in the undeformed configuration—originally coincident with $\vec{N}$.

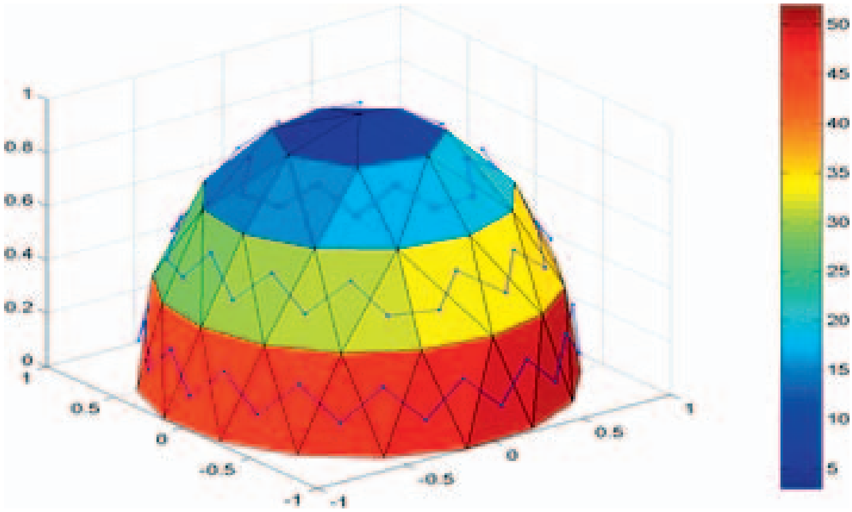

FIG. 12 — *Unit half sphere domain of integration for accumulating dissipation contributions from microkinematic elements (lines, planes) of all possible orientations.*

$$\vec{n} = \vec{N}\,\overline{\overline{F}}^{-1} \tag{10}$$

The history of length change or of shearing of a single microkinematic element (line or plane) in a single orientation is not by itself a complete indicator of dissipation. But the cumulative effects of all possible microkinematic elements can be considered by integrating over the unit half sphere representing all orientations (see Fig. 12). The dissipation contribution of each oriented line segment or material plane is computed via a dissipation law, here implemented as the Kraus law [*29*]. The dissipation law relates the extensional strain amplitude or the shear strain amplitude of the microkinematic element to its contribution to total dissipation. The amplitudes are extracted via the same rainflow counting algorithm [*30*,*31*] that is used in the fatigue analysis.

The microkinematic approach offers several advantages. Like the prior art dissipation models of Luchini et al. [*26*] or Terziyski and Kennedy [*27*], the present model avoids a full constitutive description of time-dependent stress–strain behavior and so does not require elaborate experimental or computational procedures. It also guarantees coordinate frame independence, so that dissipation calculations carried out in different reference frames give the same answer for any multiaxial loading history. The microkinematic approach shares some key features with the microsphere models [*32–34*], but again, is not a full stress–strain model and therefore avoids many of the associated computational costs and convergence risks.

Kraus Self-Heating Law

The Kraus law is convenient because it does an excellent job of capturing typical dynamic mechanical analyzer (DMA) data from the rubber lab. For the tread cap region of the tire model, published strain sweep and temperature sweep DMA results [*35*] for a carbon black (CB) filled solution styrene–butadiene rubber (SSBR) tread compound were used here (control compound in that publication). In the absence of other data, the dissipative properties of this compound were applied to all materials in the tire for the sake of simplicity.

The replotted data from this prior study and our analyses thereof are shown in Fig. 13. The storage modulus (E') exhibits the classic Payne effect [*29*,*36*] softening with respect to dynamic strain amplitude (ε_a), and the loss modulus (E'') versus ε_a shows the related peak. The strain-dependent E'' data can be captured using the Ulmer-modified Kraus model [*29*,*37*], which is one of the loss modulus functions available in Endurica CL software.

$$E''(\varepsilon_a) = E''_\infty + \frac{2(E''_{\max,K} - E''_\infty)(\varepsilon_a/\varepsilon_{a,c})^m + \Delta E''_U}{(\varepsilon_a/\varepsilon_{a,c})^{2m} + 1} \text{ where } \Delta E''_U = E''_0 - E''_\infty \quad (11)$$

The $\varepsilon_{a,c}$, m, $E''_{\max,K}$, E''_0, and E''_∞ are fitting parameters, and the values for the SSBR tread compound were determined to be 0.0131, 0.638, 2.07, 1.80, and 1.06 MPa from the fit shown in Fig. 13a.

The hysteresis h function in Endurica CL that governs self-heating of the rubber is given by:

$$h = CE''(\varepsilon_a)\varepsilon_a^2 \quad (12)$$

In this expression, the Kraus model fit provides E'' as a function of strain.

The previously published loss tangent (tan δ) results were converted to h using the following

$$h \approx \pi \tan \delta \; \sigma_a \varepsilon_a \quad (13)$$

This is valid for linear viscoelastic material with a normal sinusoidal stress output for an applied sinusoidal strain input. This is generally true for filled rubber, which exhibits "linear-nonlinear dichotomy" of viscoelastic behavior [*38*,*39*]. The stress amplitude (σ_a) is determined from the applied strain amplitude and the magnitude of the complex modulus ($|E^*|$), $\sigma_a = |E^*|\varepsilon_a$. To determine the scaling factor, C, in Eq. (12), a simple tension simulation was conducted at a strain amplitude of 0.1, and C was selected to match the simulated hysteresis with the experimental value shown by the arrow in Fig. 13c.

Temperature Sensitivity of Self-Heating Law

Temperature and strain rate dependence of the hysteresis can be implemented in the Endurica material definition via a modification of Eq.

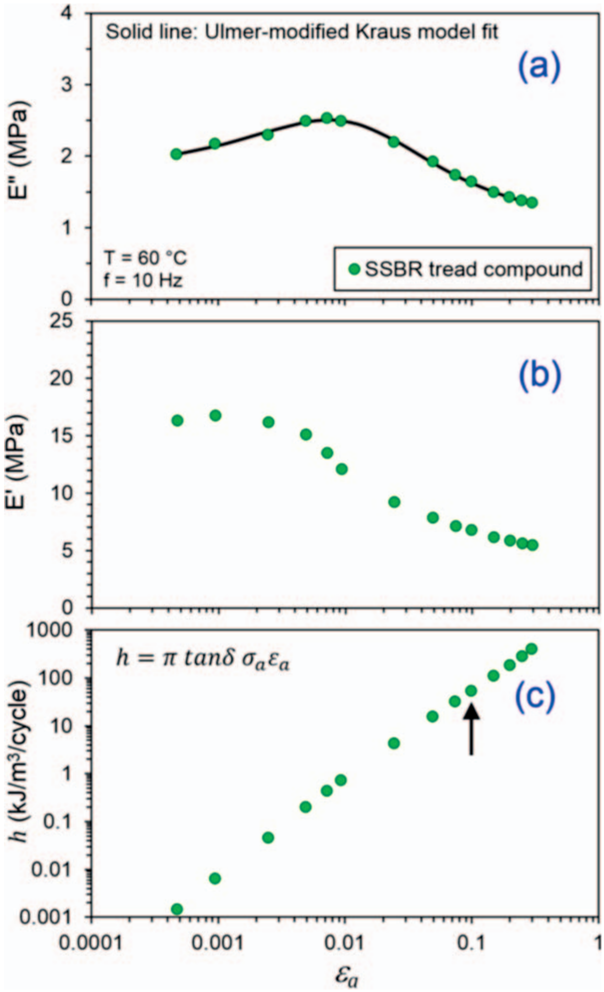

FIG. 13 — *Dynamic mechanical data for SSBR tread compound (control) from strain sweep ((a) to (c)), adapted from Warasitthinon and Robertson [35]. (a) Fit of the Ulmer-modified Kraus model to the loss modulus vs strain amplitude data. (b) Typical strain-dependent softening of the storage modulus (Payne effect). (c) Arrow indicates the point used to calibrate the hysteresis function in Endurica CL software (quantify scaling factor, C).*

(12) that follows Terziyski et al. [*27*], given below. Herein, the strain rate ($\dot{\varepsilon}$) dependence of hysteresis, relative to the reference strain rate, $\dot{\varepsilon}_0$, is assumed to be negligible ($Z = 0$). The value of $r = -0.0110$ 1/°C, which describes the temperature (θ) dependence of hysteresis relative to the reference temperature θ_0, was determined from the temperature sweep data shown in Fig. 14.

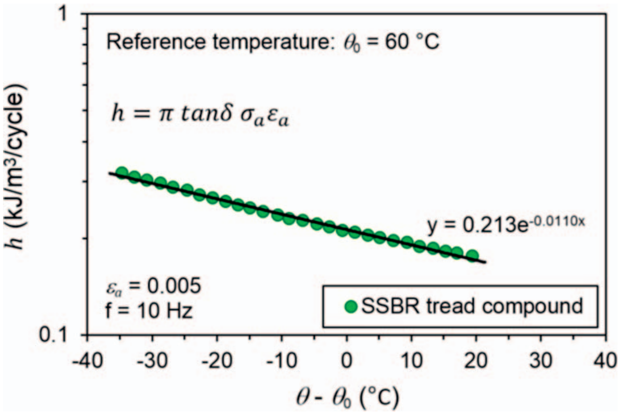

FIG. 14 — *Exponential fit to the temperature sweep results gives the coefficient of temperature dependence,* r*, for the hysteresis function in Endurica CL software.*

$$h = CE''(\varepsilon_a)\varepsilon_a^2 e^{r(\theta-\theta_0)+Z(\dot{\varepsilon}-\dot{\varepsilon}_0)} \tag{14}$$

Thermal Analysis Workflow

The steady-state thermal analysis workflow executed for each of the steady-state structural solutions obtained is shown in Fig. 15. Owing to the nonlinear dependence of the dissipation rate on temperature that is implicit in Eq. (14), the workflow implemented iterations where strain and temperature fields were passed from Abaqus to Endurica, and dissipation fields were passed from Endurica to Abaqus. Iterations continued until the steady-state temperature fields computed in Abaqus were consistent with the temperature-dependence dissipation fields computed in Endurica. Rolling resistance was also computed for each simulation by integrating the dissipation field over the volume of the tire to obtain a total dissipation $\dot{Q}$ and solving the relationship $\dot{Q} = F_{rr}V$ for the rolling resistance force F_{rr} given tire rolling speed V.

Thermal Results

For each steady-state thermal solution, both the total rolling resistance and the temperature distribution were computed. Figure 16 shows the rolling resistance dependence on test step. Figure 17 (left) shows the dependence on speed. Below approximately 200 kph for this tire, the rolling resistance shows little dependence on speed. In fact, up until 160 kph, there appears to be a very slight decrease in rolling resistance, possibly due to growth of the tire diameter under increasing inertial forces. Increasing inflation pressure is commonly known to produce diameter growth and decrease rolling resistance [*40*,*41*]. Perhaps the effect of increased tire speed is in certain ways similar to increasing

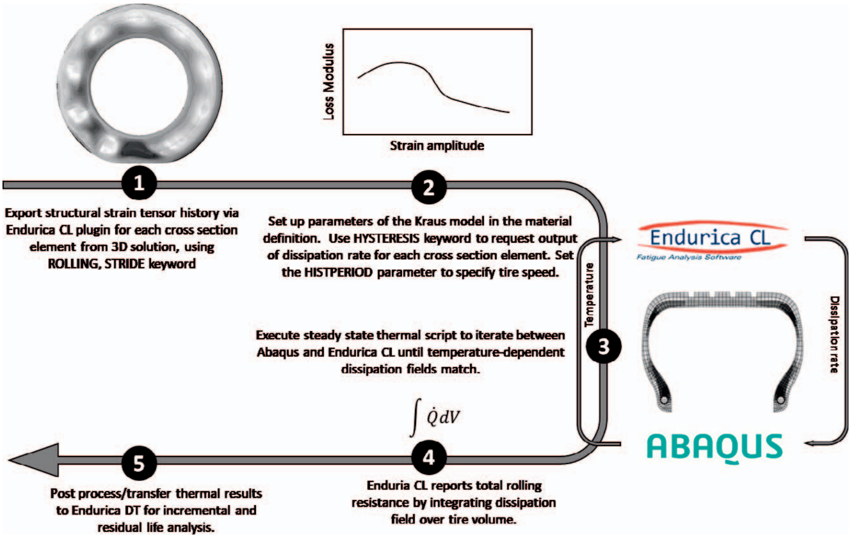

FIG. 15 — *Steady-state thermal analysis workflow.*

inflation pressure. Beyond step 9 of the test, however, there is a rapid increase in rolling resistance. This is clearly associated with development of the standing wave. The rolling resistance of the tire on a roadwheel is shown to be somewhat higher than on a flat road surface, as has been reported many times in past. Removing the overwrap has only a slight effect on tire rolling resistance.

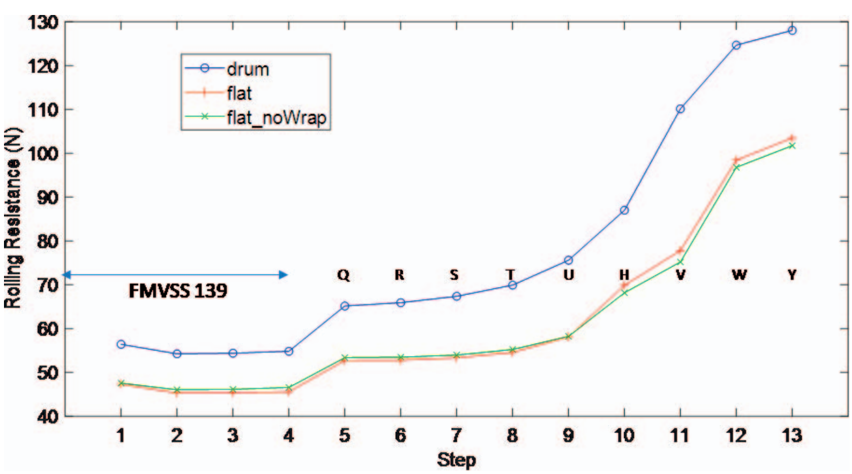

FIG. 16 — *Steady-state rolling resistance at each step of the procedure.*

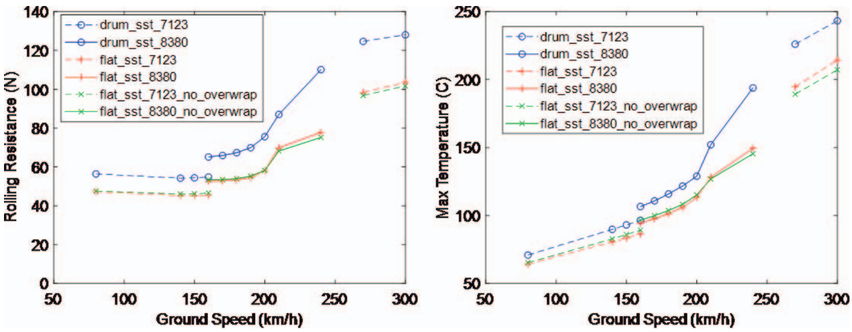

FIG. 17 — *(left) Rolling resistance dependence on speed. (right) Peak tire temperature dependence on speed.*

Maximum temperature in the tire, shown in Fig. 17 (right), increases at first on a linear trend with regard to speed but gives way to stronger increases at high speed once the standing wave develops. Temperatures on the 1.7 m road wheel drum were significantly higher than temperatures on a flat road surface, as observed previously [*42*]. Only very slight operating temperature differences are predicted for the comparison of tires with and without overwrap, and there seems to be a crossover in ranking as tire speed increases.

The temperature distributions for drum and flat road cases on the tire cross section are plotted in Fig. 18 for 80, 200, and 300 kph. Again, it is apparent that the drum case runs hotter, especially in the tire shoulder and the lower sidewall. Presumably this is associated with the larger deflection attained at constant load on the drum. It is also apparent that increasing tire speed increases tire operating temperature. Temperatures are also plotted vs test step for the critical belt,

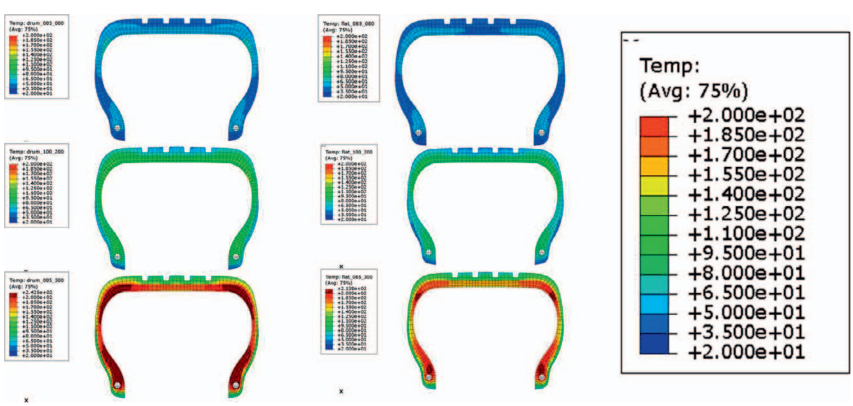

FIG. 18 — *Steady-state temperatures on (left) drum and (right) flat road surfaces for (top to bottom) 80, 200, and 300 kph.*

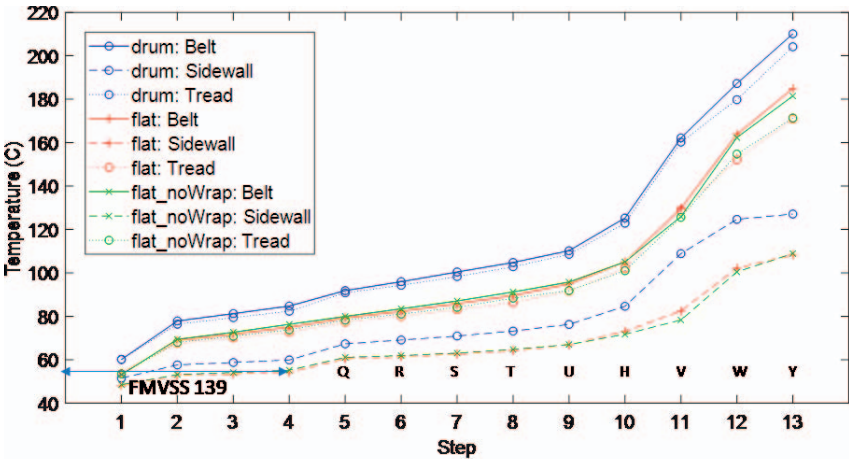

FIG. 19 — *Steady-state temperatures for critical belt, sidewall, and tread elements.*

sidewall, and tread elements in Fig. 19. The locations for these critical elements are shown in Fig. 20.

Durability Analysis

Once strain and temperature fields were generated for the steady-state rolling tire at each step of the testing protocol, an assessment was then made of durability. The assessment considers the fracture mechanical properties [*43–49*] of the rubber compounds. The analysis is based on the incremental, critical plane framework available in Endurica DT and the steady-state rolling feature in Endurica CL. Together, these tools account for the potential development of cracks in all elements of the tire, over the scheduled series of load cases. They also enable the calculation of residual life following the conclusion of each step.

Material Behavior

In addition to stress–strain and thermal properties discussed previously, durability analysis requires knowledge of the crack growth rate law of each compound. The basic material models, including strain-crystallization effects, have been described in prior work [*50*]. Owing to the strong temperature dependence on speed, it is essential in addition to consider how the crack growth rate law depends on temperature.

Crack growth rate law and temperature dependence. According to Thomas [*44*], the fatigue crack growth rate r in rubber follows a power law dependence on the energy release rate T.

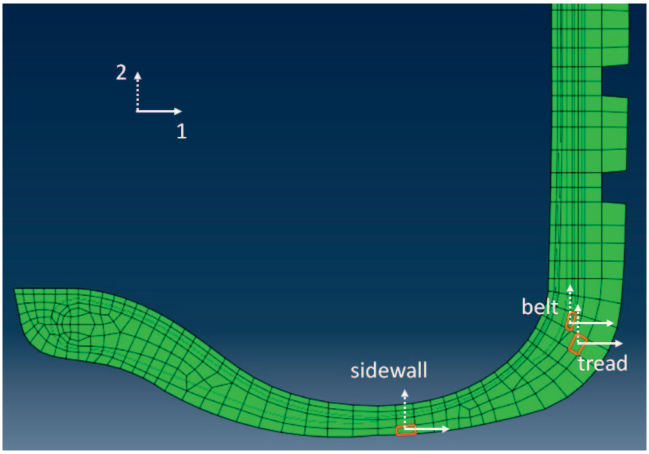

FIG. 20 — *Locations and local element coordinate system definitions for worst case elements.*

$$r = r_c\left(\frac{T}{T_c(\theta)}\right)^F \tag{15}$$

The material parameters are the fracture mechanical strength T_c, the power law slope F, and the value of the crack growth rate r_c, at which the power law intersects a vertical asymptote placed at T_c. We give in Table 3 a summary of the parameter values chosen for each tire compound in this analysis. In all cases, $r_c = 1 \times 10^{-2}$ mm/cyc has been used.

TABLE 3 — *Material properties at reference temperature for fatigue analysis.*

No.	Name	Material	C_{10} (Mpa)	T_c @25 °C, kJ/m^2	F_0	C_0, mm
1	Inner liner	Rubber	0.64	38.3	2.98	0.025
2	Abrasion	Rubber	1.71	16.0	2.0	0.001
3	Bead	Steel	—	—	—	—
4	Apex	Rubber	3.63	285	2.0	0.030
5	Shoulder	Rubber	1.79	285	2.0	0.010
6	Body ply	Nylon	—	—	—	—
7	Ply gum	Rubber	1.79	285	2.0	0.010
8	Edge cover	Rubber	4.06	120	2.0	0.100
9	Tread	Rubber	1.04	20.75	4.95	0.100
10	Inner belt	Steel	—	—	—	—
11	Outer belt	Steel	—	—	—	
12	Belt gum	Rubber	4.06	120	2.0	0.100
13	Overwrap	Nylon	—	—	—	—
14	Tread base	Rubber	4.06	164	2.0	0.008

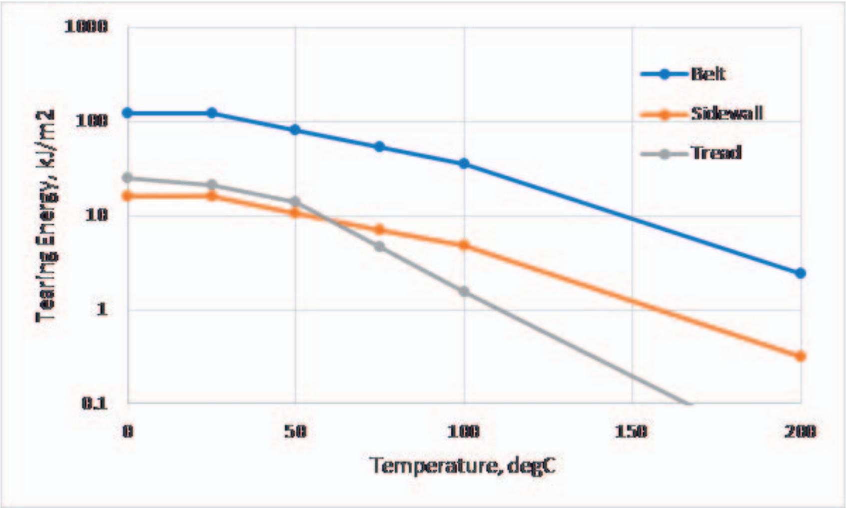

FIG. 21 — *Durability analysis workflow for first two test steps.*

The Endurica material model permits any of the parameters in Eq. (15) to be defined as an arbitrary, tabular function of temperature. Based on the work of Young [*45*], it seems that letting the strength parameter T_c depend on temperature, while regarding F and r_c as constant, can be justified as a first approximation, and this has been applied herein. This scheme offers perhaps the most inexpensive path for characterizing the temperature effect on the crack growth rate law. One simply makes a series of strength measurements over the temperature range of interest. Here, Young's results were used to construct the tabular definitions shown in Fig. 21. The results for 200 °C have been extrapolated from the lower temperatures. The Endurica material model syntax for specifying temperature-dependent fracture strength T_c for the belt is simply:

$$\text{Fatigue\_Temps} = 0.000,\ 25.000,\ 50.000,\ 75.000,\ 100.000,\ 200.000$$

$$\text{Tcritical} = 120.00,\ 120.00,\ 80.00,\ 53.33,\ 35.55,\ 2.40$$

Crack precursor size. The analysis assumes that crack precursors exist at all points in the model. Crack precursors have elsewhere been identified as having sizes c_0 in the range $10 \times 10^{-3} < c_0 < 100 \times 10^{-3}$ mm [*51–54*]. The initial size of the precursor is an important parameter that must be specified for each material. In practice, precursor size should be calibrated so as to enforce the agreement between the crack growth rate law integration shown in Eq. (16) and the known results of a cycles-to-crack fatigue experiment either on a test coupon or on the tire itself. The cycles-to-crack experiment will produce a life N when growing a crack precursor from initial size c_0 to end-of-life size c_f. We have used here $c_f = 1$

mm. In practice, so long as $c_0 \ll c_f$, the computed life N is insensitive to the choice of c_f.

$$N(\theta, \varphi\ ) = \int_{c_0}^{c_f} \frac{dc}{r(T)} \tag{16}$$

The variables θ and φ in Eq. (16) specify the orientation of the critical plane, which for fully relaxing, simple tension experiments will be oriented perpendicular to the loading direction.

Critical Plane Analysis

Critical plane analysis has been described in detail in earlier reports [*55–62*]. Critical Plane Analysis evaluates potential crack growth at every point in the tire, for every possible orientation a crack might take. In the Endurica CL total formulation, critical plane analysis computes, for each possible point and orientation, the number of repeats N_f of a given duty cycle that are required to grow the crack precursor from its original size c_0 to the size c_f marking the end of life. The calculation is iterated over all possible values of θ and φ, taking care to identify the particular orientation that minimizes the life prediction. In this sense, critical plane analysis produces the most conservative possible interpretation of the damaging effects for a given stress/strain history.

In evaluating Eq. (16) for variable amplitude histories, it is necessary to identify the constituent constant amplitude events that together produce the total crack growth rate. This is accomplished by means of a rainflow counting operation that is performed on the energy release rate history estimated for the plane specified by θ and φ. The rainflow counting and damage summation operation is iterated for all planes, so that the finally selected critical plane truly reflects the most damaging possible experience across all planes and events. For cases of proportional tension/shear loading, the critical plane method tends to predict cracking aligned with the maximum principle stress direction. For other cases, however, other crack orientations appear as most damaging. In cases of compression and shear, for example, crack closure causes the critical plane to occur with an orientation that maximizes shearing of the crack. It has been shown [*63*] that critical plane analysis accurately predicts the “sideways” orientation of cracks appearing under nonrelaxing loads in strain-crystallizing rubbers.

Incremental Analysis

Multistep durability tests require an incremental procedure to accumulate the damage occurring at each step of the test. In particular, Eq. (16) is no longer applicable—it applies in the case of a single duty cycle that is repeated ad infinitum until end of life, but we need to reformulate our damage integration rule in order to accommodate the feature that the load case may change as a function of applied cycles. The reformulation is presented in Eq. (17), and implemented in Endurica DT. Equation (17) uses the same crack growth rate laws and input variables as before, but the variable of integration is now cycles rather than crack size [*64*].

$$\Delta c_{i\rightarrow i+1,j,k} = \int_{N_i}^{N_{i+1}} r\Big(T(\theta,\varphi,N)\Big)dN \tag{17}$$

In this formulation, the crack growth rate law r is integrated from the beginning of cycle N_i to its final cycle N_{i+1}. The result of the integration is the change of length of a crack $\Delta c_{i\rightarrow i+1,j,k}$ for each plane j and element k of the model. The accumulated crack lengths for each element are written to a file during the analysis, so that future additions of load history may begin at the point at which the prior increment left off. In this scheme, there is no requirement that the duty cycle during one increment be the same as the duty cycle in subsequent increments. The crack length may be updated in as many increments as are needed to represent the testing schedule. The combination of the critical plane analysis with the incremental solution method is quite powerful, enabling accurate damage accounting of arbitrary compositions of multiaxial, variable amplitude loading history.

From the user perspective, the incremental workflow is implemented as a series of successive Endurica DT analyses, each with its own load case and RESTART output request specifying the number of repeats to be applied for the step.

Residual Life Calculations

A special case of the incremental analysis yields the residual life calculation. In order to quantify remaining life at any given step, a nominal metric duty cycle may be defined (in the present study, 85% load at 80 kph has been used), and the number of repeats of this nominal cycle is computed for the hypothetical case where the nominal cycle is repeated ad infinitum until end of life (when the crack reaches length c_f), starting with the damage state/crack length existing at the end of step i.

Endurica DT returns the residual life when the initial damage state of the model is set to the state recorded in the restart file from the end of the history. To compute residual life, the integration is continued from the end of the history until end of life is reached.

Durability Analysis Workflow

Figure 22 illustrates the workflow that was used for analysis of the high-speed durability testing protocol. Each step of the protocol was first divided into two substeps in order to approximately address the thermal transience of each

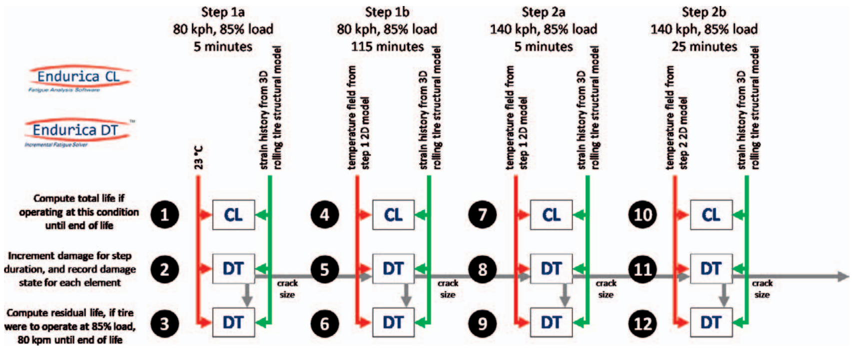

FIG. 22 — *Critical tearing energy dependence on temperature for belt, sidewall, and tread compounds.*

step. The first substep in all cases had a duration of 5 minutes and was computed using the temperature field from the prior step. The second substep covered the remainder of the total step duration using the steady-state temperature field from the current step. Within each step, three durability calculations were made. First, the total life for the current step was computed with Endurica CL. This calculation gives the total number of tire revolutions required to reach end of life in the case that the tire operates at constant load and speed equal to the current step. Second, the damage state (i.e., crack length in each element) at the end of each step was computed using Endurica DT's implementation of Eq. (17) to integrate from the crack size at the end of the prior step to the crack size at the end of the current step. These results are written to a restart file that is later used to start integration of the subsequent step. Third, the residual life remaining following the end of the present step was computed with Endurica DT, again using Eq. (17) but now allowing the upper limit of integration to run out to end of life. For this calculation, the first step of the protocol is used as a reference load case. In other words, we compute tire revolutions under step 1 loading that would be required to grow the crack from the end of the step to end of life.

Durability Results

The fatigue analysis identified critical regions of the tire in the belt gum, in the sidewall, and in the tread material. The critical elements are shown on the tire cross section in Fig. 20. Each element is displayed with its local element coordinate system. The local element coordinate systems were generated by copying the global system, so that the 1 (x) direction points toward the right, and the 2 (y) direction points upward.

For each of the critical elements, the distribution of fatigue life over all orientations is visualized via the damage sphere, as shown in frames b, c, and d

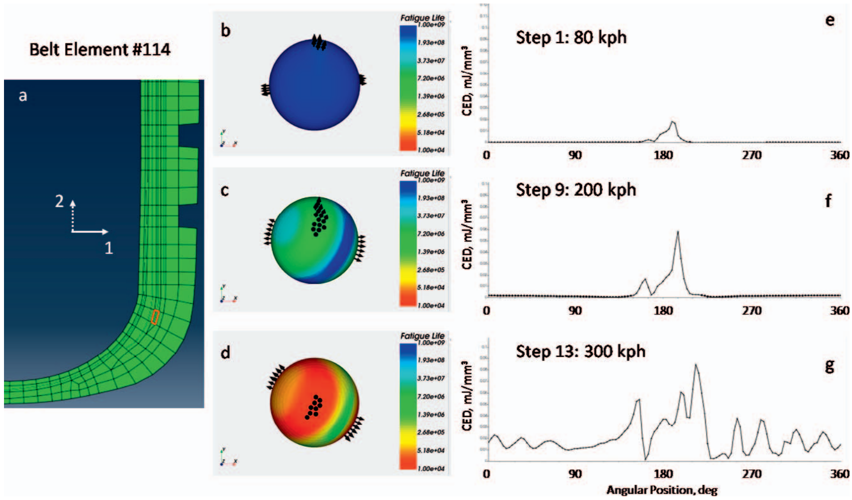

FIG. 23 — *(b–d) Damage spheres showing distribution of life with regard to orientation for worst case belt edge element (located at element shown in a). (e–g) History of cracking energy density on the critical plane at the belt edge.*

of Figs. 23–25. On the damage sphere, red represents orientations with shortest life, and blue represents orientations with longest life. Outward pointing vectors are drawn on each sphere to represent the normal to the most favorable cracking planes. Note that the sphere orientation in these figures matches the coordinate system shown in frame a. The history of cracking energy density on the most critical plane is also plotted for each case in frames e, f, and g. Generally, all of the histories show that at low speed, a single load–unload cycle occurs as material passes through the tire footprint (centered at 180 degrees). With increased speed, the magnitude of the cracking energy density increases, and the development of standing waves produces multiple load–unload events per tire revolution. In order to properly account for damaging effects of such histories, a rainflow counting algorithm is necessary to identify the individual event pairs to be used in computing the maximum and minimum of each cycle and the crack growth rate of each cycle. Most of the histories are seen to be fully relaxing, with the notable exception of the belt edge at high speed. At high speed, the standing wave imposes many nonrelaxing cycles of significant amplitude on the belt edge. This result suggests that the strain-crystallization properties of the belt gum compound, which are apparent under nonrelaxing cycles, may be especially relevant at high speed.

The belt edge and tread element results show that there are two simultaneous critical planes situated at roughly 90 degrees from each other. This result is typical of a fully reversed simple shearing deformation cycle,

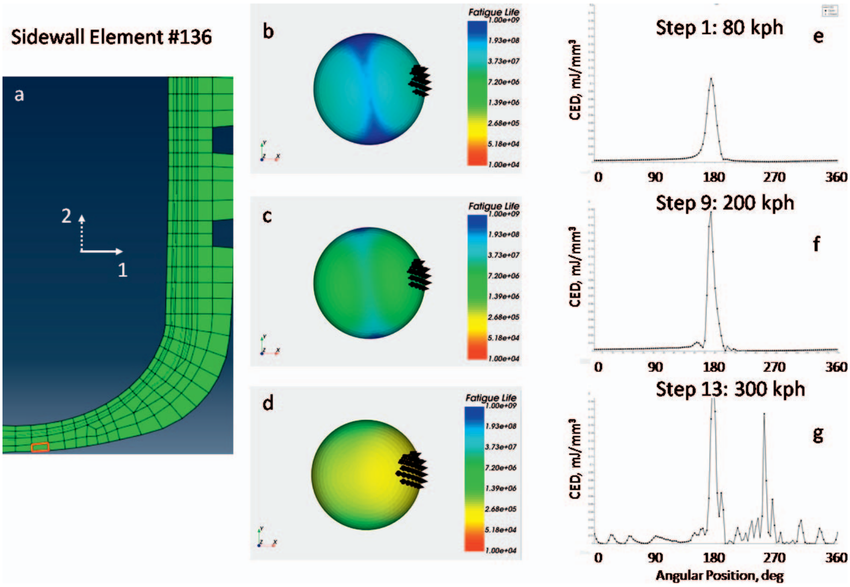

FIG. 24 — *(b–d) Damage spheres showing distribution of life with regard to orientation for worst case sidewall element (located at element shown in a). (e–g) History of cracking energy density on the critical plane at the worst sidewall element.*

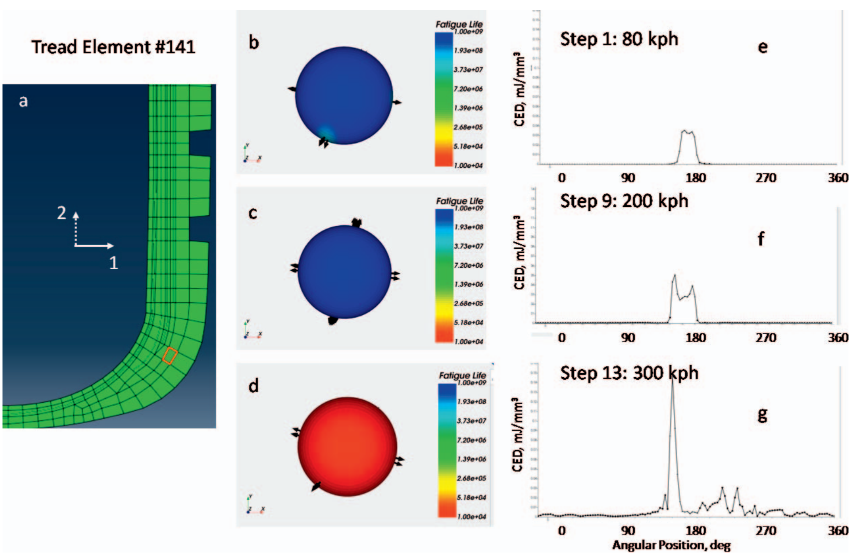

FIG. 25 — *(b–d) Damage spheres showing distribution of life with regard to orientation for worst case tread element (located at element shown in a). (e–g) History of cracking energy density on the critical plane at the worst case tread element.*

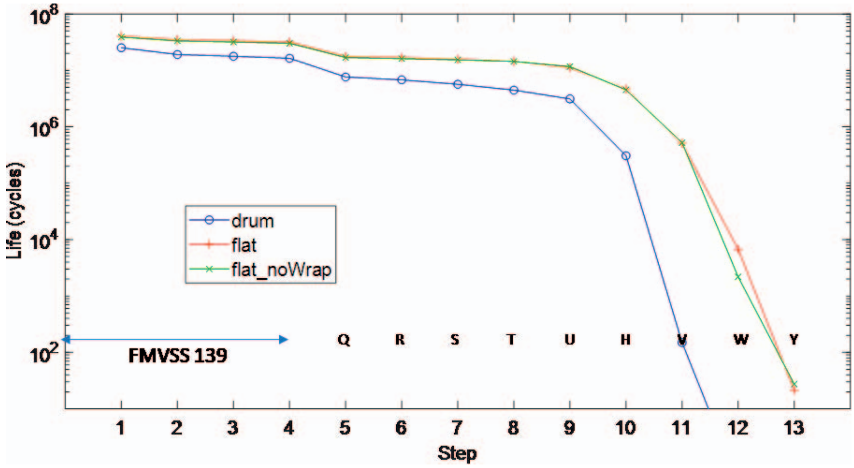

FIG. 26 — *Revolutions to 1 mm crack, under the assumption that entire life is spent operating at the step's load and speed.*

consistent with the expected deformations associated with flattening of a curved composite beam (i.e., the belt package). The belt element shearing seems most pronounced in the 1–3 plane, and the tread element shearing in the 1–2 plane. The sidewall element results show a single critical plane that is oriented along the tension direction.

Prior to executing the Endurica DT incremental workflow to accumulate damage across all load cases, it is useful to execute the Endurica CL total workflow to understand the fatigue life of each individual load case on its own. The results of these total fatigue life calculations, for each step applied on its own, is shown in Fig. 26. The results shown are for the belt edge element, which was the most critical. The onset of the standing wave is seen to strongly reduce the life that would be expected at each step, to the point that the life is reduced to 100 cycles by step 11 for the drum road wheel case, and by step 13 for the flat road surface case. The strong reduction in life owes both to the strong decrease of tearing energy with temperature and to the multiplication of deformation cycles per tire revolution and its associated impact on tire operating temperature. The results are plotted vs speed in Fig. 27. If one were to apply Miner's rule using these results, the damage rate per cycle would be equal to one per life from these results. Therefore, the inverse of life can be viewed approximately as a measure of damage rate per cycle. The significant decrease of life at step H corresponds to development of the standing wave and indicates an increase of damage rate in going from U to H of an order of magnitude and in going from H to V of 4 orders of magnitude!

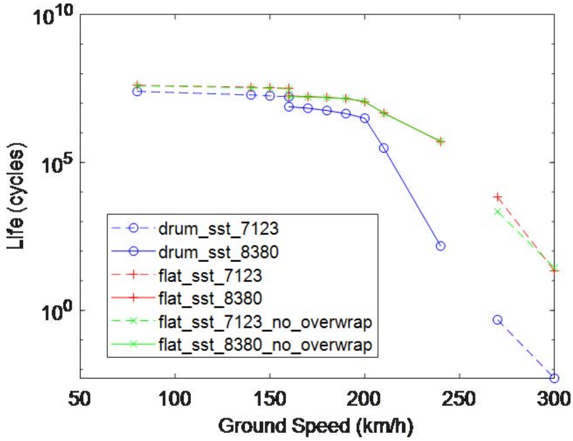

FIG. 27 — *Revolutions to 1 mm crack as a function of tire speed, under the assumption that entire life is spent operating at the step's load and speed.*

The final incremental analysis with Endurica DT is shown in Figs. 28 and 29. The incremental analysis takes account of the test step durations applied. For purposes of analysis, and in order to approximately represent the thermal transient at each step, each step was broken into two increments. The first increment had a duration of 5 minutes and was simulated using the steady-state temperature field of the prior step. The second and final increment of each step was run for the remaining duration of each step and was simulated using the

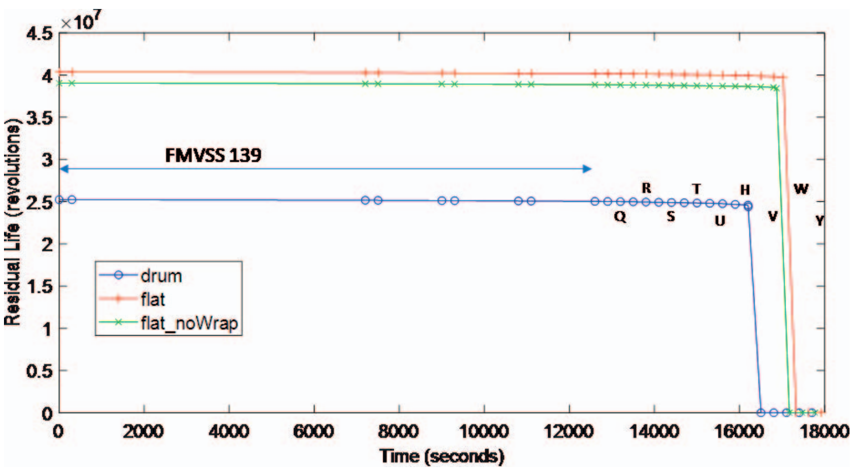

FIG. 28 — *Residual life (in revolutions at step 1 conditions) remaining as a function of test time.*

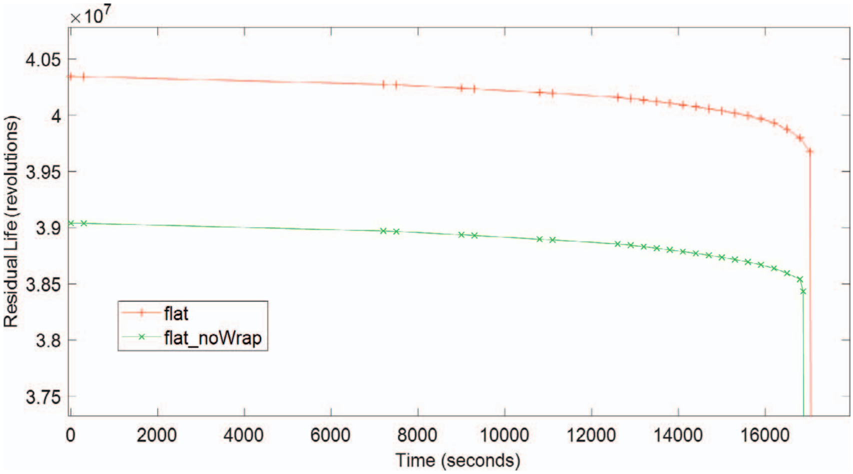

FIG. 29 — *Same results as in last figure, but with zoomed-in scale on residual life.*

steady-state temperature field of the step. The life that is reported here is the residual life, computed in terms of repeats of the first load case of the series that would be endured following the steps applied up to that point in the history. Because the initial load steps are so light relative to the capacity of the tire, and because the steps have such short durations relative to the potential life under those conditions, it can be seen that initial steps in the testing do very little to reduce the residual life of the tire.

Expanding the ordinate scale in Fig. 29 shows the progressive degradation occurring throughout the test. Comparing these results with those of the structural and thermal analyses suggests that the acceleration of residual life reduction commences with the development of the standing wave. The effects of the standing wave are quite severe, owing to the multiplication of load–unload cycles per tire revolution, to the strong increase in self-heating and operating temperature, and to the strong decrease of compound strength (and increase of crack growth rate) with increasing temperature. The combination of these factors leads to a precipitous drop of residual life following development of the standing wave. On the road wheel test, this tire is predicted to achieve a speed rating of H. The impact of running the protocol on a flat road surface in lieu of the 1.7 m road wheel is predicted to be an increase from H to V, suggesting that the drum testing does provide a margin of safety relative to the labeling of the tire. For the overwrap vs no overwrap comparison simulated, it is predicted that the tire with overwrap will exhibit marginally better endurance than the tire without overwrap. The margin, however, in the particular case simulated, amounts to less than what would be needed to attain a higher speed rating, just a few minutes or a few tens of kilometers.

Conclusion

The incremental, critical plane fatigue analysis procedures of Endurica DT, combined with the improved convergence at high speed of Abaqus 2019, now make possible the analysis of multistep, high-speed durability schedules with greater detail and accuracy than previously possible.

Tire materials exhibit many “special effects” that must be captured in order to make a proper accounting of damage accrual. The strain amplitude dependence of the viscoelastic loss modulus was specified via the Kraus model with quite high accuracy. For high-speed tests, thermal effects triggered in association with standing waves were shown to dominate, and the temperature dependencies of the viscoelastic and fracture strength laws exhibited a particularly strong influence on the speed rating achieved in the simulation. The table-lookup functions of the Endurica DT incremental solver are especially convenient for accurately capturing such effects.

The effects of standing waves on predictions of rolling resistance and operating temperature are consistent with previously reported behavior. In particular, the weak dependence of rolling resistance on speed below the standing wave speed was predicted, and the strong increase of dissipation associated with development of standing waves was successfully predicted. Also, the higher rolling resistance of curved vs flat was successfully predicted.

Incremental critical plane analysis of the regulatory high-speed tests provides, for the first time, estimates of the relative damage contribution of each test step and of the residual life following each step. The results suggest that rather little damage is done to the tire in a high-speed test until the very last test steps finally produce strong thermal-induced weakening of the tire materials combined with strongly increasing temperatures.

While the present workflow has incorporated instantaneous temperature dependence in the structural, thermal, and fatigue analysis, it did not fully account for thermal transients and it did not account for any thermochemical changes in material properties due to ageing effects. The incremental framework is fully capable of representing these details, however, and future development of the workflow can be aimed at incorporating these effects as well.

References

[1] United States Department of Transportation National Highway Traffic Safety Association [DOT NHTSA], “Laboratory Test Procedure for FMVSS No. 139 – New Pneumatic Radial Tires for Light Vehicles,” TP-139-02, January 6, 2006. Available at https://www.nhtsa.gov/sites/nhtsa.gov/files/tp-139-02.pdf. Accessed August 11, 2021.

[2] United Nations Economic Commission for Europe [UN ECE], "Uniform Provisions Concerning the Approval of Pneumatic Tyres for Motor Vehicles and Their Trailers," United Nations, March 29, 2007. Available at https://unece.org/fileadmin/DAM/trans/main/wp29/wp29regs/r030r3e.pdf. Accessed August 11, 2021.

[3] De Eskinazi, J., Ishihara, K., Volk, H., and Warholic, T. C., "Towards Predicting Relative Belt Edge Endurance with the Finite Element Method," *Tire Science and Technology*, Vol. 18, 1990, pp. 216–235.

[4] Ebbott, T. G., "An Application of Finite Element-Based Fracture Mechanics Analysis to Cord-Rubber Structures," *Tire Science and Technology*, Vol. 24, 1996, pp. 220–235.

[5] Wei, Y. T., Tian, Z. H., and Du, X. W., "A Finite Element Model for the Rolling Loss Prediction and Fracture Analysis of Radial Tires," *Tire Science and Technology*, Vol. 27, 1999, pp. 250–276.

[6] Govindjee, S., "Firestone Tire Failure Analysis," 2001. Available at http://faculty.ce.berkeley.edu/sanjay/REPORT_Secure.PDF. Accessed August 11, 2021.

[7] Han, Y. H., Becker, E. B., Fahrenthold, E. P., and Kim, D. M., "Fatigue Life Prediction for Cord-Rubber Composite Tires Using a Global-Local Finite Element Method," *Tire Science and Technology*, Vol. 32, 2004, 23–40.

[8] Yin, H. S., Hu, Y. S., Zhang, H., Yang, M. M., and Wei, Y. T., "Truck Tire Thermal-Mechanical FEA and DMA with Application to Endurance Evaluation," *Tire Science and Technology*, Vol. 34, 2006, pp. 220–236.

[9] Kaliske, M., Näser, B., and Meiners, C., "Inelastic Fracture Mechanics for Tire Durability Simulations." *Tire Science and Technology*, Vol. 35, 2007, pp. 239–250.

[10] Ozelo, R. R. M., Sollero, P., and Costa, A. L. A., "An Alternative Technique to Evaluate Crack Propagation Path in Hyperelastic Materials," *Tire Science and Technology*, Vol. 40, 2012, 42–58.Viscoelasticity

[11] Kim, S., Park, H., Moon, B., Sung, K., Koo, J.-M., and Seok, C.-S., "The Prediction Methodology for Tire's High Speed Durability Regulation Test Using a Finite Element Method," *International Journal of Fatigue*, Vol. 118, 2019, pp. 77–86. Available at: https://www.sciencedirect.com/science/article/pii/S0142112318304602. Accessed August 11, 2021.

[12] Padovan, J., "On and Standing Waves in Tires." *Tire Science and Technology*, Vol. 4, 1976, pp. 233–246.

[13] Padovan, J., "On Standing Waves in Tires," *Tire Science and Technology*, Vol. 5, 1977, pp. 83–101.

[14] Chatterjee, A., Cusumano, J. P., and Zolock, J. D., "On Contact-Induced Standing Waves in Rotating Tires: Experiment and Theory," *Journal of Sound and Vibration*, Vol. 227, 1999, pp. 1049–1081.

[15] Cho, J. R., Kim, K. W., and Jeong, H. S., "Numerical Investigation of Tire Standing Wave Using 3-D Patterned Tire Model," *Journal of Sound and Vibration*, Vol. 305, 2007, pp. 795–807.

[16] Nakajima, Y., "Standing Waves in Tires," in Nakajima, Y. (ed.), *Advanced Tire Mechanics*, Springer, Singapore, 2019, pp. 1129–1157.

[17] Marlow, R. S., "A General First-Invariant Hyperelastic Constitutive Model," *Constitutive Models for Rubber*, Proceedings of the 3rd European Conference on Constitutive Models for Rubber, London, 2003, pp. 157–160.

[18] Qi, J., Herron, J. R., Sansalone, K. H., Mars, W. V., Du, Z. Z., Snyman, M., and Surendranath, H., "Validation of a Steady-State Transport Analysis for Rolling Treaded Tires," *Tire Science and Technology*, Vol. 35, 2007, pp. 183–208.

[19] Garcia, M. A., Kaliske, M., Wang, J., and Bhashyam, G., "A Consistent Implementation of Inelastic Material Models into Steady State Rolling," *Tire Science and Technology*, Vol. 44, 2016, pp. 174–190.

[20] van der Steen, R., Lopez, I., Nijmeijer, H., Schmeitz, A. J. C., and de Bruijn, B., "Experimental and Numerical Study of Friction and Braking Characteristics of Rolling Tires," *Tire Science and Technology*, Vol. 39, 2011, pp. 62–78.

[21] Olatunbosun, O. A. and Bolarinwa, O., "FE Simulation of the Effect of Tire Design Parameters on Lateral Forces and Moments," *Tire Science and Technology*, Vol. 32, 2004, pp. 146–163.

[22] SIMULIA, "2019 FD03 Documentation," Dassault Systèmes, Providence, RI, 2019.

[23] Walter, J. D. and Conant, F. S., "Energy Losses in Tires," *Tire Science and Technology*, Vol. 2, 1974, pp. 235–260. (gives effect of speed on RR).

[24] Whicker, D., Browne, A. L., Segalman, D. J., and Wickliffe, L. E., "A Thermomeehanical Approach to Tire Power Loss Modeling," *Tire Science and Technology*, Vol. 9, 1981, pp. 3–18. (gives effect of speed on RR).

[25] LaClair, T. J. and Zarak, C., "Truck Tire Operating Temperatures on Flat and Curved Test Surfaces," *Tire Science and Technology*, Vol. 33, 2005, pp. 156–178.

[26] Luchini, J. R., Peters, J. M., and Arthur, R. H., "Tire Rolling Loss Computation with the Finite Element Method," *Tire Science and Technology*, Vol. 22, 1994, pp. 206–222.

[27] Terziyski, J. and Kennedy, R., "Accuracy, Sensitivity, and Correlation of FEA-Computed Coastdown Rolling Resistance," *Tire Science and Technology*, Vol. 37, 2009, pp. 4–31.

[28] Mars, W. V. and Luchini, J. R., "An Analytical Model for the Transient Rolling Resistance Behavior of Tires," *Tire Science and Technology*, Vol. 27, 1999, pp. 161–175.

[29] Kraus, G., "Mechanical Losses in Carbon-Black-Filled Rubbers," *Journal of Applied Polymer Science: Applied Polymer Symposium*, Vol. 39, 1984, pp. 75–92 (1984).

[30] Society of Automotive Engineers, "SAE Fatigue Design Handbook: AE-22," Society of Automotive Engineers, Warrendale, PA, 1997.

[31] ASTM, "Standard Practices for Cycle Counting in Fatigue Analysis," E1049-85, American Society for Testing and Materials Standards, West Conshohocken, PA, 1985.

[32] Diani, J., "Directional Constitutive Laws for Rubbers," *Rubber Chemistry and Technology*, Vol. 89, 2016, pp. 22–31.

[33] Johlitz, M., Dippel, B., and Lion, A., "Dissipative Heating of Elastomers: A New Modelling Approach Based on Finite and Coupled Thermomechanics," *Continuum Mechanics and Thermodynamics*, Vol. 28, 2016, pp. 1111–1125.

[34] Khalalili, L., Azad, A. I., Lin, J., and Dargazany, R., "Modular Platform to Model Parallel Inelastic Mechanisms in Rubber-Like Materials," *Rubber Chemistry and Technology*, Vol. 92, 2019, pp. 51–68.

[35] Warasitthinon, N. and Robertson, C. G., "Interpretation of the tan δ Peak Height for Particle-Filled Rubber and Polymer Nanocomposites with Relevance to Tire Tread Performance Balance," *Rubber Chemistry and Technology*, Vol. 91, 2018, pp. 577–594.

[36] Payne, A. R., "The Dynamic Properties of Carbon Black-Loaded Natural Rubber Vulcanizates. Part I," *Journal of Applied Polymer Science*, Vol. 6, 1962, pp. 57–63.

[37] Ulmer, J. D., "Strain Dependence of Dynamic Mechanical Properties of Carbon Black-Filled Rubber Compounds," *Rubber Chemistry and Technology*, Vol. 69, 1996, pp. 15–47.

[38] Randall, A. M. and Robertson, C. G., "Linear-Nonlinear Dichotomy of the Rheological Response of Particle-Filled Polymers," *Journal of Applied Polymer Science*, Vol. 131, 2014, pp. 40818-1–40818-10.

[39] Xiong, W. and Wang, X., "Linear-Nonlinear Dichotomy of Rheological Responses in Particle-Filled Polymer Melts," *Journal of Rheology*, Vol. 62, 2018, pp. 171–181.

[40] Cohn, A., "Commercial Trailer Tires: Tire Inflation and Its Effect on Rolling Resistance, Fuel Economy, and Tire Footprint," *Tire Science and Technology*, Vol. 43, 2015, pp. 144–162.

[41] Bachman, L. J., "Do Changes in Temperature and Inflation Pressure Affect Rolling Resistance during Road and Track Testing for Fuel Economy of Class 8 Tractor-Trailers?" *Tire Science And Technology*, Vol. 46, 2018, pp. 93–104.

[42] LaClair, T. J. and Zarak, C., "Truck Tire Operating Temperatures on Flat and Curved Test Surfaces," *Tire Science and Technology*, Vol. 33, 2005, pp. 156–178.

[43] Rivlin, R. S. and Thomas, A. G., "Rupture of Rubber. I. Characteristic Energy for Tearing," *Journal of Polymer Science*, Vol. 10, 1953, pp. 291–318.

[44] Thomas, A. G., "Rupture of Rubber. V. Cut Growth in Natural Rubber Vulcanizates," *Journal of Polymer Science*, Vol. 31, 1958, pp. 467–480.

[45] Young, D. G. and Danik, J. A., "Effects of Temperature on Fatigue and Fracture," *Rubber Chemistry and Technology*, Vol. 67, 1994, pp. 137–147.

[46] Lake, G. J., "Application of Fracture Mechanics to Crack Growth in Rubber-Cord Laminates," *Rubber Chemistry and Technology*, Vol. 74, 2001, pp. 509–524.

[47] Gent, A. N. and Mars, W. V., "Chapter 10 – Strength of Elastomers," in Mark, J. E., Erman, B., and Roland, M. (eds.), *The Science and Technology of Rubber,* 4th ed., Academic Press, Boston, 2013, pp. 473–516, ISBN 9780123945846, 10.1016/B978-0-12-394584-6.00010-8.

[48] Mars, W. V., "Fatigue Life Prediction for Elastomeric Structures," *Rubber Chemistry and Technology*, Vol. 80, 2007, pp. 481–503.

[49] Näser, B., Kaliske, M., and Mars, W. V., "Fatigue Investigation of Elastomeric Structures," *Tire Science and Technology*, Vol. 38, 2010, pp. 194–212.

[50] Mars, W. V., Wei, Y., Hao, W., and Bauman, M. A., "Computing Tire Component Durability via Critical Plane Analysis," *Tire Science and Technology*, Vol. 47, 2019, pp. 31–54.

[51] Gent, A. N., Lindley, P. B., and Thomas, A. G., "Cut Growth and Fatigue of Rubbers. I. The Relationship Between Cut Growth and Fatigue," *Journal of Applied Polymer Science*, Vol. 8, 1964, pp. 455.

[52] Huang, Y. S. and Yeoh, O. H., "Crack Initiation and Propagation in Model Cord-Rubber Composites," *Rubber Chemistry and Technology*, Vol. 62, 1989, pp. 709–731.

[53] Choi, I. S. and Roland, C. M., "Intrinsic Defects and the Failure Properties of Cis-1, 4-Polyisoprenes," *Rubber Chemistry and Technology*, Vol. 69, 1996, pp. 591–599.

[54] Li, F., Liu, J., Mars, W. V., Chan, T. W., Lu, Y., Yang, H., and Zhang, L. Q., "Crack Precursor Size for Natural Rubber Inferred from Relaxing and Non-Relaxing Fatigue Experiments," *International Journal of Fatigue*, Vol. 80, 2015, pp. 50–57.

[55] Mars, W. V., "Multiaxial Fatigue Crack Initiation in Rubber," *Tire Science and Technology*, Vol. 29, 2001, pp. 171–185.

[56] Barbash, K. P. and Mars, W. V., "Critical Plane Analysis of Rubber Bushing Durability under Road Loads," No. 2016-01-0393. SAE Technical Paper, 2016.

[57] Zine, A., Benseddiq, N., Abdelaziz, M., Hocine, N., and Bouami, D., "Prediction of Rubber Fatigue Life under Multiaxial Loading," *Fatigue & Fracture of Engineering Materials & Structures*, Vol. 29, 2006, pp. 267–278.

[58] Zarrin-Ghalami, T. and Fatemi, A., "Multiaxial Fatigue and Life Prediction of Elastomeric Components," *International Journal of Fatigue*, Vol. 55, 2013, pp. 92–101.

[*59*] Zarrin-Ghalami, T. and Fatemi, A., "Cumulative Fatigue Damage and Life Prediction of Elastomeric Components," *Fatigue & Fracture of Engineering Materials & Structures*, Vol. 36, 2013, pp. 270–279.

[*60*] Mars, W. V., "Cracking Energy Density as a Predictor of Fatigue Life under Multiaxial Conditions," *Rubber Chemistry and Technology*, Vol. 75, 2002, pp. 1–17.

[*61*] Mars, W. V., "Method and Article of Manufacture for Estimating Material Failure due to Crack Formation and Growth," U.S. Patent No. 6,634,236, October 21, 2003.

[*62*] Aït-Bachir, M., Mars, W. V., and Verron, E., "Energy Release Rate of Small Cracks in Hyperelastic Materials," *International Journal of Non-Linear Mechanics*, Vol. 47, 2012, pp. 22–29.

[*63*] Ramachandran, A., Wietharn, R. P., Mathew, S. I., Mars, W. V., and Bauman, M. A., "Critical Plane Selection Under Nonrelaxing Simple Tension with Strain Crystallization," Presented at the Fall 192nd Technical Meeting of the Rubber Division, ACS, Cleveland, OH, October 10–12, 2017 (Paper #E15).

[*64*] Mars, W. V., Suter, J. D., and Bauman, M., "Computing Remaining Fatigue Life Under Incrementally Updated Loading Histories," No. 2018-01-0623. SAE Technical Paper, 2018.